Programmable Interface Asymmetric Integration of Carbon Nanotubes and Gold Nanoparticles toward Flexible, Configurable, and Surface-Enhanced Raman Scattering Active All-In-One Solar-Driven Evaporators

Chang Zhang, Peng Xiao,* Feng Ni, Yanping Yang, Jincui Gu, Lei Zhang, Junyuan Xia, Youju Huang, Wenqin Wang,* and Tao Chen*

With the rapid development of industrialization and urbanization, water pollution and water shortage are increasingly serious problems. Detecting potential contaminants and further extracting purified water from polluted water is considered to be an effective way for sewage management and recycling. Herein, an all-in-one solar-driven evaporator is developed by alternatively depositing carbon nanotube (CNT) films and gold nanoparticle films on flexible cotton fabric surfaces for both solar-driven pollution detection and water collection. Based on the facile and robust interfacial self-assembly strategy, a large-area CNT film at the air/water interface and closely packed Au nanoparticle (AuNP) film assembled at the liquid/liquid interface are readily achieved, which can be further alternatively transferred onto the cotton fabric surface for solar-to-thermal conversion applications. Owing to the favorable flexibility and foldability of the cotton fabric, the CNT film–modified cotton enables the configurable transition from a 2D flat structure to adjusted 3D wave-like structures for enhanced solar steam generation. Furthermore, when the AuNP film is further deposited onto the surface of the CNT film for polluted water evaporation, the resultant CNT-loaded Au hybrid can realize effective pollutant detection through surface-enhanced Raman scattering (SERS) signals.

1. Introduction

The continuous shortage and pollution of clean water have severely restricted the development of modern society and quality of life, which have led to growing demands of sewage detection and treatment.[1,2] Although water purification techniques have played significant roles in handling water contamination, the effective detection of the varieties of contaminants enables better estimation of the effects on human health and environment, which also provides a considerable basis for further purification technologies.[3] As a renewable and sustainable resource, solar energy has been immensely exploited to realize energy storage and photo-to-thermal conversion applications.[4–7] As the conventional solar-driven bulk water evaporation suffers from low energy efficiency, the interfacial evaporation technology targeted at localizing heat in the water evaporation surface has attracted tremendous attention due to its high efficiency.[8,9] Over the past few years, considerable advances have been achieved to develop a series of photothermal materials, such as plasmonic nanostructures,[10–15] carbon nanomaterials,[16–22] functional polymers,[23–25] biomass source materials,[26–28] etc.

However, up till now, most of the researches have focused on the fabrication of high-performance water evaporators or pollutant detectors. The separate functional devices have caused some issues, such as high cost, complicated detecting procedures, etc., which may severely limit practical applications. As a result, an all-in-one device is highly desired. More recently, Zhu and coworkers developed a dual functional solar evaporator for both water purification and pollution detection by asymmetrically introducing the 3D self-assembly of plasmonic silver nanoparticles into the nanoporous alumina template. The effective combination of these two functions has opened up a new avenue to realize multifunctional evaporators.[29] Despite achieving this significant advancement, this integration strategy for producing the all-in-one evaporator is highly preferred in practical applications. In

C. Zhang, Prof. W. Wang
School of Materials Science and Chemical Engineering
Ningbo University
Ningbo 315211, China
E-mail: wangwenqin@nbu.edu.cn

C. Zhang, Dr. P. Xiao, F. Ni, Y. Yang, J. Gu, Dr. L. Zhang, J. Xia, Dr. Y. Huang, Prof. T. Chen
Key Laboratory of Marine Materials and Related Technologies
Zhejiang Key Laboratory of Marine Materials and Protective Technologies
Ningbo Institute of Material Technology and Engineering
Chinese Academy of Sciences
Zhongguan West Road 1219, 315201 Ningbo, China
E-mail: tao.chen@nimte.ac.cn; xiaopeng@nimte.ac.cn

Dr. P. Xiao, F. Ni, Dr. L. Zhang, Dr. Y. Huang, Prof. T. Chen
School of Chemical Sciences
University of Chinese Academy of Science
Beijing 100049, China

The ORCID identification number(s) for the author(s) of this article can be found under https://doi.org/10.1002/ente.201900787.

**ADVANCED
SCIENCE NEWS**
www.advancedsciencenews.com

Energy Technology
Generation, Conversion, Storage, Distribution
www.entechnol.de

addition, the development of diverse systems for multifunctional evaporators can also assist in practical applications.

2. Results and Discussions

The schematic illustration of the all-in-one solar-driven evaporator is shown in **Figure 1**a, in which water with the trace pollutant is effectively extracted to the surface of the Au/CNTs fabric (ACF) driven by the solar-enhanced wicking effect. As a result, the ACF can function as both a solar steam generator and a surface-enhanced Raman scattering (SERS)-active pollutant detector under sunlight. As shown in Figure 1b, the large-area CNT film is self-assembled at the air/water interface via the Marangoni effect and capillarity-driving compression approach.[30–32] Subsequently, the as-prepared film was transferred onto the fabric surface with controlled thickness via multiple transfer procedures. The resultant photothermal fabric experienced configurable structures from a flat 2D state to a wave-like 3D state,[33] resulting in enhanced water evaporation due to effective space utilization toward the vertical direction. Prior to the AuNP film deposition, the —COOH-functionalized CNT film was decorated with poly(ethylenimine) (PEI) to further receive the AuNPs with negative charges under acidic conditions. Furthermore, the AuNP film assembled at the hexane/water interface was attached onto the PEI-modified CNT surface, which made the ACF favorable for pollutant detection by the SERS signals. In our system, the CNT films and plasmonic AuNP films can be asymmetrically modified onto the cotton fabric surface to achieve dual functions in a programmable and efficient way, allowing the production of multifunctional solar-to-thermal devices.

The commercially available cotton fabric is flexible and foldable, which is endowed with knitted and fibrous structures. From the scanning electron microscopy (SEM) images, it was observed that the tightly intertwined structure could provide a well-controlled rough surface to enhance the photothermal property and also enable the desirable capillarity for water absorption (Figure S1, Supporting Information). As shown in Figure S2, Supporting Information, the water uptake test was conducted, in which the methylene blue aqueous solution was selected to mark the level of water absorption. The result clearly demonstrated that the cotton fabric was equipped with favorable water absorption capabilities. To achieve a large-area CNT film in a facile and efficient way, the interfacial self-assembly strategy was used at the air/water interface via spray coating and subsequent porous sponge-induced compression method (Figure S3, Supporting Information). The interfacial Marangoni spread allows the formation of homogenous preassembled CNT films on the water surface, followed by a capillary force driving compression for the closely packed CNT network (**Figure 2**a). When transferred onto the cotton fabric surface, a uniform CNT/fabric hybrid can be readily achieved (Figure 2b). After the drying process at an ambient condition, the flexible CNT-modified fabric in a large scale could be further folded into desired shapes. Even though the resultant fabric experienced rigorous folding procedures, it could still maintain good stability without apparent CNT delamination (Figure 2c,d). Moreover, the achieved fabric enables multiple transfers of CNT films, resulting in a series of fabric hybrids with well-controlled thickness. As shown in Figure 2e, fabrics with two, four, six, eight, and ten layers of CNT films were readily acquired. With the increase in CNTs' film layers, the surface of the cotton fabric tended to become much rougher (Figure S4, Supporting Information). Owing to the desirable foldable features of the cloth, the CNT films could be alternatively transferred onto the specific location of the cotton substrate by alternatively folding the other parts of the cloth fabric (Figure 2e). Microscopically, SEM characterization was adopted to investigate
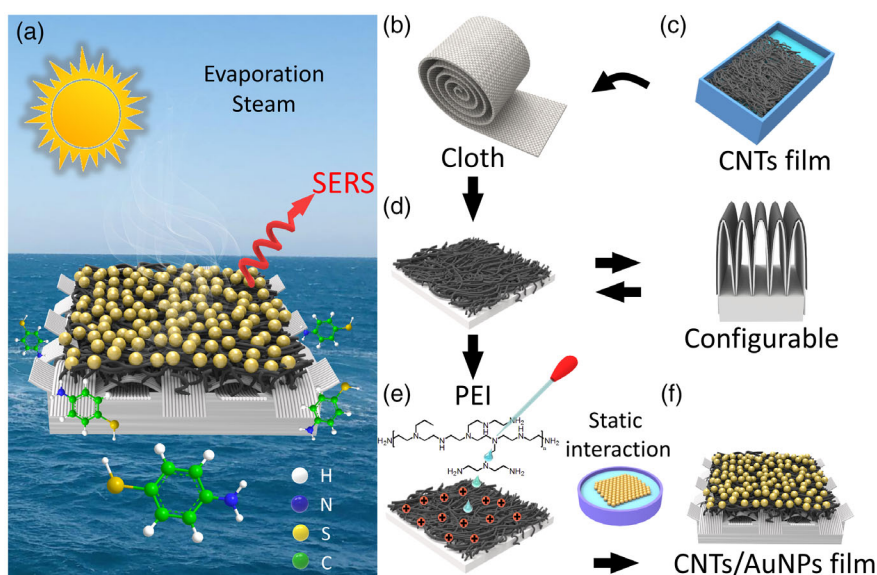
Figure 1. a) Schematic illustration of the all-in-one solar-driven evaporator. b) The interfacial self-assembly of the CNT film at the air/water interface. c) The resultant CNT film was further transferred onto the cotton fabric surface. d) The CNT-modified fabric can experience a configurable transition from the 2D to 3D state. e) The CNT side of the fabric was further decorated with the PEI polymer using the drop-coating method. f) The assembled Au film at the hexane/water interface was finally deposited onto the CNT film surface for SERS-active solar evaporator.
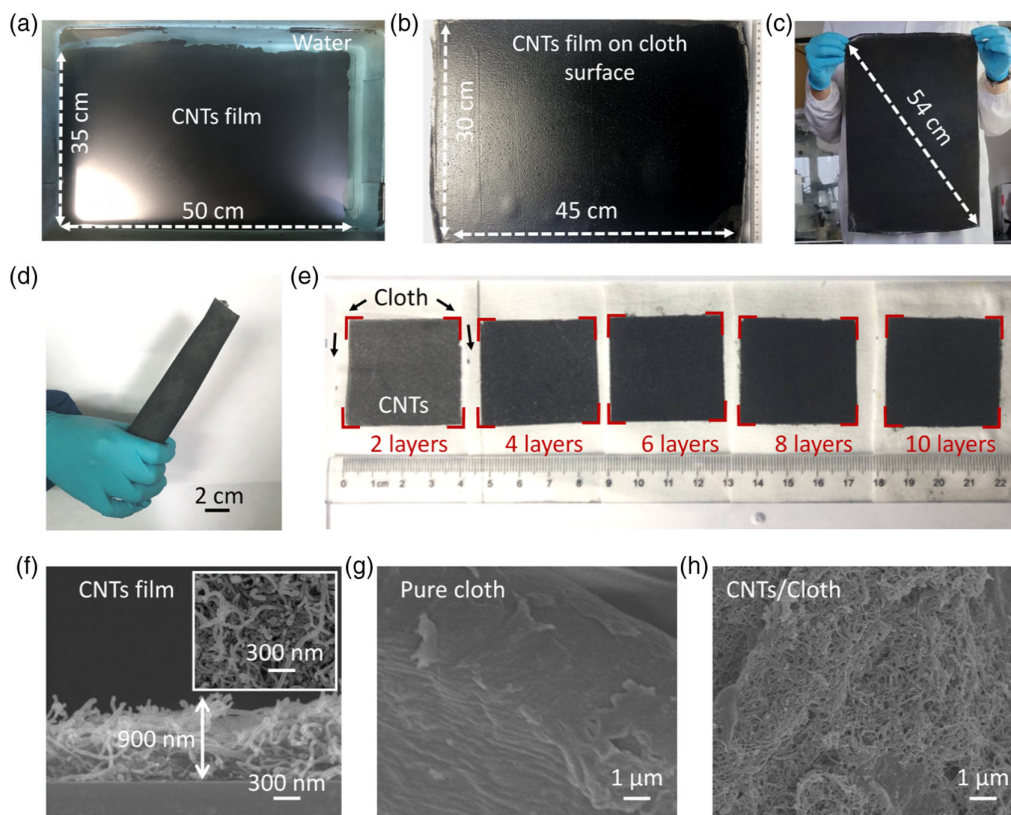
Figure 2. a) The CNT film was self-assembled at the air/water interface. b) The resultant CNTs film was transferred onto the cloth surface. c) Photograph of dried CNT-modified fabric. d) The resultant hybrid fabric is flexible and foldable. e) Cloth fabric was asymmetrically modified with CNT films with a series of thickness. f–h) SEM images of the cross section of a one-layer CNT film. Inset: The surface morphology of the f) CNT film, g) cotton fabric, and h) CNT-modified fabric.

the microstructures of the as-prepared samples. As shown in Figure 2f, the thickness of the assembled CNT film at the air/water interface can reach up to about 900 nm. Compared with the smooth surface of the original cotton fabric, the CNT-modified cotton surface presented a relative smooth surface with a porous tubular network (Figure 2g,h).

As the CNT films can be alternatively transferred using the alternative folding method, patterned CNT films on the cotton fabric with two cotton-based tails were fabricated. As shown in **Figure 3**a, the fabric was attached onto the polystyrene foam surface, in which two tails were in contact with bulk water for water pumping. This asymmetric structure can also effectively reduce the thermal conduction to the bulk water. As an efficient photothermal material, CNT films with a relatively rough surface can effectively reduce the reflectance. With the increase in CNT film layers ranging from two to ten, compared with the high reflectance, the as-prepared fabric demonstrated a gradual decrease in the reflectance to a lowest value of ≈2% (Figure 3b). As a result, the light absorption of the fabric with increased CNT layers represented a prominent tendency to increase, which can reach up to more than 90% in the wavelength range from 400 to 2500 nm (Figure 3c). The increased light absorption of the CNT-modified fabric can remarkably transform solar energy to heat, which can prominently elevate the surface temperature of the fabric. It was observed that when the layers of the

deposited CNT films were more than four layers, the achieved light absorption approaches a stable value. From Figure 3c, it is found that the value of light absorption of the fabric with six CNT layers is slightly lower than that of the fabric with eight CNTs layers. Note that the fabric with six CNTs layers was chosen to conduct further measurements due to considerable light absorption.

Superior to the bulk water with a 2 °C rise in temperature within 12 min under 1 sun, the CNT-modified one showed a prominent improvement of surface temperature from 18 to 51 °C in the same condition (Figure 3d,e). Meanwhile, it was found that the generated heat was mostly confined to the photothermal layer of the fabric. Furthermore, the vertical temperature distribution was also measured, which strongly evidenced the extremely low thermal conduction to the bulk water (Figure 3f,g). In addition, water contact angle (WCA) measurements were also conducted to explore the ability of water absorption. (Figure 3h). For the original fabric, the cotton fabric can effectively absorb the water droplet within 15 s. Whereas, for the fabric with six CNT layers, the capillary pores generated by the CNT network can prominently enhance the capillarity of the resultant fabric, resulting in faster water absorption within only 0.5 s. Nevertheless, it should be considered that excess CNT layers may severely reduce the size of the pores inside the CNT network, which can severely limit water transportation. As a result, solar-driven evaporation
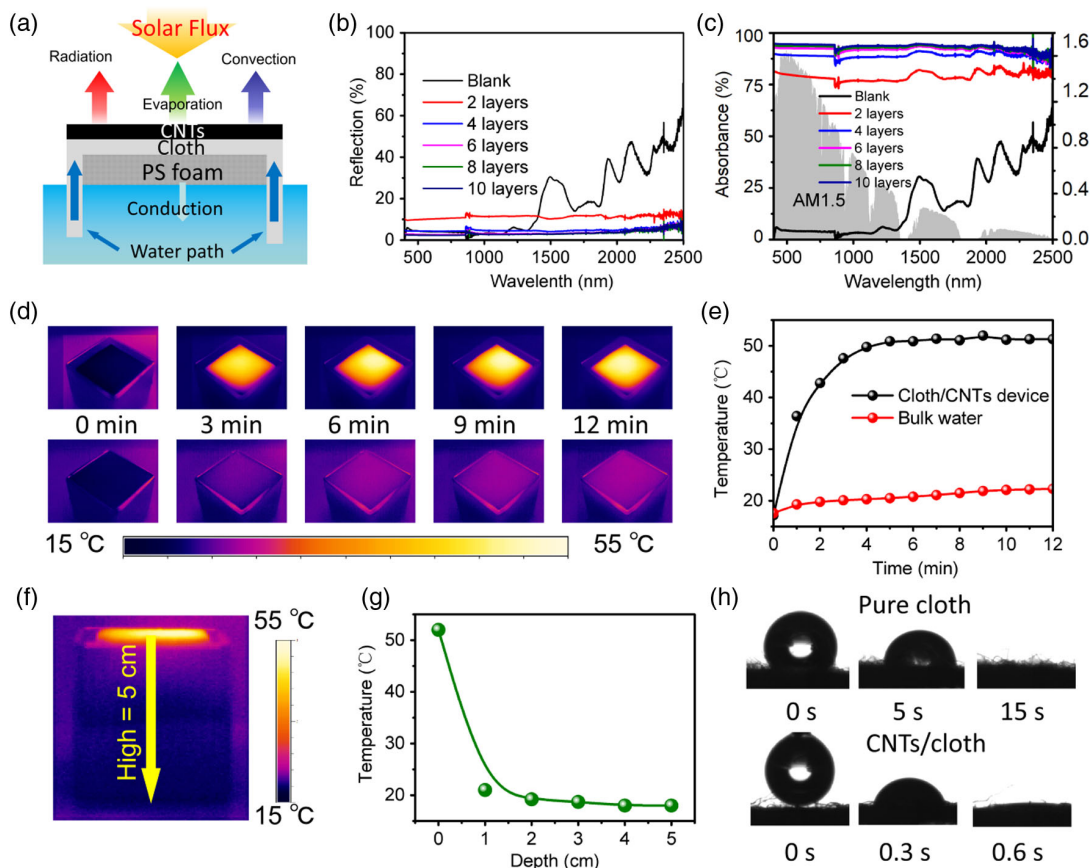
Figure 3. a) The evaporation mechanism of the flat 2D evaporator with two cotton tails for water pumping. b) Reflectance and c) absorption versus wavelength curves of original cotton fabric and CNT-modified fabric with different thicknesses of CNT films. d) IR images of the surface temperature for both bulk water and photothermal fabric of six CNT film layers with different illumination times under 1 sun. e) The corresponding surface temperature versus time curves of bulk water and photothermal fabric. f) IR image of the vertical temperature distribution of the CNT-modified fabric floated on the water surface. g) The temperature versus depth curve. h) Static water angle (WCA) of pure cotton fabric and CNT-modified fabric.

experiments were used to investigate the optimal layers of CNT films.

For solar-to-thermal conversion applications, the solar simulator and the corresponding apparatus are schematically illustrated in **Figure 4**a. To further explore the optimum CNT layers, water evaporation experiments in the lab were conducted. The weight loss of the fabric with different CNT layers over time under 1 sun illumination is recorded in Figure 4b. Superior to bulk water, the CNT-modified fabric samples presented higher weight loss. With the increase in the CNT layers, water evaporation showed a parabola-like tendency, in which the fabric with six layers demonstrated an optimal performance (Figure 4c). The result may be derived from the reduced water transportation channels for CNT-modified fabrics with more than six layers. Furthermore, a series of repeated experiments were performed to investigate the stability of the fabric with six CNTs layers, which strongly evidenced the good repeatability of the optimized solar evaporators (Figure 4d). In addition, the surface temperature of the cotton fabric with six CNTs layers was also investigated under simulated solar intensity ranging from 0.5 to 2.5 sun. As displayed in Figure S5, Supporting Information, the stabilized temperature represented a gradual increasing tendency from 37.4 at 0.5 sun to 70.7 °C at 2.5 sun. To further investigate the capability of the solar evaporator performance under different light intensities, the relative mass change curves under light intensity from 0.5 to 2.5 sun are recorded and shown in Figure 4e. The results demonstrated that there was a linearly positive correlation between evaporation rates and light intensity, ranging from 0.717 to 3.985 $kg\,m^{-2}$, which ensured good adaptability in changeable environments (Figure 4f). In our system, the evaporation efficiency is defined as $\eta = mh/I$,[34] in which m denotes mass flux, h is the total enthalpy of the liquid/liquid sensible heat from the initial temperature to equilibrium temperature and liquid/vapor latent heat, and I is the input power of solar illumination. As a result, the calculated efficiency presented a gradual increase from 80% to 90% (Figure 4g). Furthermore, even under a higher simulated light intensity of up to 10 $kW\,m^{-2}$, water steam can also be clearly observed, enabling continuous and stable water evaporation (Figure 4h). As shown in Figure 4i, the concentrations of six ions of Na^+, Ca^{2+}, Mg^{2+}, K^+, Sr^{2+}, and B^{3+} were prominently reduced, which are lower than that of the World Health Organization (WHO) standard, indicating potential applications in purified water collection.
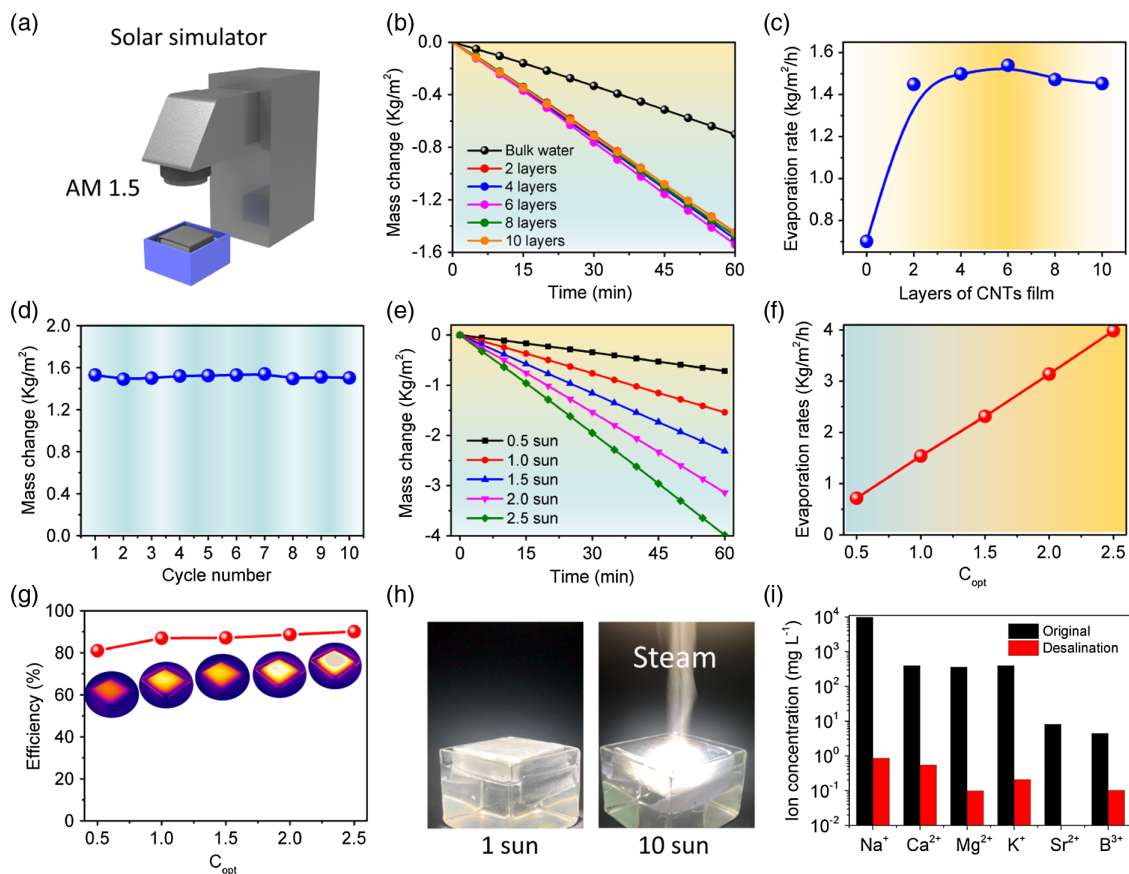
Figure 4. a) The sketch of the solar light simulator. b) Mass change versus time curves of bulk water and fabrics with a series of CNT layers under 1 sun illumination. c) Evaporation rate versus CNT film layers' curve, demonstrating a maximum value of six layers. d) The evaporation tests of optimal six CNT layers of the fabric were conducted several times with good repeatability. e) Mass change versus time curves of the optimal fabric under different simulated sunlight intensities from 0.5 to 2.5 sun. f) The corresponding evaporation rate versus light intensity curve with a linearly positive correlation tendency. g) The calculated efficiency versus light intensity curve. h) Photos of water steam generated under 1 and 10 sun. i) The ion concentration of six simulated seawater samples before and after desalination.

Since the flat 2D structure has low space utilization toward the vertical direction, the design of the 3D structure is considered to effectively improve water evaporation performance.[35] Specifically, the as-prepared CNT-modified cotton fabric can be folded into a variety of 3D structures, such as a five-pointed star, bamboo, airplane, cone, and boat (Figure S6, Supporting Information). To further explore the evaporation performance of the 3D evaporators with adjustable structures, as a proof of concept, the CNT-modified fabric could be transformed from the 2D structure to a wave-like 3D one by a simple folding technique.[36] As schematically illustrated in Figure S7, Supporting Information, the 3D shape of the photothermal fabric was fixed using a stainless steel mesh, which could be folded into desirable shapes. It is noted that compared with the other 3D structure, the wave-like one can be readily adjusted by increasing the numbers of waves. To investigate the effects of the numbers of waves on evaporation rates, a series of CNT-modified fabric samples ranging from 1 to 7 waves were fabricated (**Figure 5**a). As shown in Figure 5b,c, with the increase in waves, the calculated water evaporation rates represented a parabola-like tendency. With the continuous increase in waves, the distance between the two adjacent waves decreased

gradually. As a result, less recessed parts of the 3D structure were exposed to solar light, demonstrating reduced water evaporation performance. For the same projected area and wave height, excess waves could lead to the decreased active area of light absorption. Nevertheless, the ratio of height to width of the 3D structure is also considered to be an important factor that can remarkably affect the resultant performance of the solar evaporators. In our experiments, to investigate how the numbers of waves influence water evaporation, the height and width of the 3D structure are strictly fixed to a constant. It is noted that the ratio of height to width is beyond the scope of this work. It is expected that the optimized ratio can also significantly affect the evaporation performance, which will be carefully studied in future work.[37] In addition, the effect of the incident angle on water evaporation for the 3D system is also discussed in our system. Specifically, for the 2D system, the entire surface can be always covered by incident solar light with variable angles and the received energy can experience a dynamic change process. However, for the wave-like 3D structure, the changeable incident angle may have a relatively complex impact on the final performance of the 3D one. It may derive from the specific spatial 3D structure, in which only the partial surface

can be covered by sunlight under practical conditions. Note that compared with the 2D structure, with the change of incident angles, some parts of the 3D structure can realize a vertical incidence for enhanced solar absorption under nonvertical incidence. As a result, it is considered to be a complicated process, which can be further explored in future work. However, to effectively decrease the effect of incident angles on 3D evaporation, a symmetric structure can be rationally designed to acquire a desirable evaporation performance. In our system, we also fabricated a hierarchical and symmetric 3D configuration to extensively receive solar light from changeable incident angles (Figure S8, Supporting Information). Note that a theoretical simulation can be further introduced to construct solar evaporators with favorable environmental adaptability.

Significantly, the maximum evaporation rate of the optimized 3D structure reached up to $2.186 \, kg \, m^{-2} \, h^{-1}$, which was higher than that of the 2D structure; the potential mechanism was also explored in our system. Note that the top layer of the 3D structure was defined as the basal plane to measure the solar intensity. The 3D structure with five waves was selected to measure the stabilized surface temperature under 1 sun. As shown in Figure 5d, the temperature of the 3D structure was ≈45 °C, which was much higher than that of bulk water. Nevertheless, from the IR images of the 3D structure with five waves, it was found that the equilibrium temperature of the 3D structure was ≈7.5 °C lower than that of the 2D one under the same condition within 12 min (Figure 5e and Figure S9, Supporting Information). In

our system, to realize a 3D structure toward the vertical direction of the space, the apex angle of the waves was generated. The resultant nonuniform incident light causes the lower surface temperature of the 3D structure, in which the heat loss can be efficiently reduced. Furthermore, the bottom parts of the 3D structure with lower temperature can gain energy from the environment. As a result, the 3D structure demonstrates a higher evaporation rate than that of the 2D one.[38,39]

To explore the performance of solar steam generators in practical applications, the outdoor experiments were also conducted. As shown in Figure S10, Supporting Information, a concept of a purified water collector was designed, in which a sloping roof and corresponding container were fabricated to acquire condensed clean water. It is noted that different from the evaporation rate calculated in the lab based on the vapor evaporated, the collected clean water in the outdoor experiments was weighed to acquire the evaporation value. For the control experiments, the planar 2D structure and 3D wave-like structure were both fixed onto the same size polystyrene foam (Figure S11a, Supporting Information). The evaporation chamber is schematically illustrated in Figure S11b, Supporting Information. In the outdoor experiments, the 2D structure and 3D one were respectively sealed into home-made chambers under natural sunlight (Figure S11c, Supporting Information). After 1 h of illumination, superior to the planar 2D structure, more condensed water droplets were observed on the chamber roof of the 3D structure (Figure S11d, Supporting Information). The weather was partly
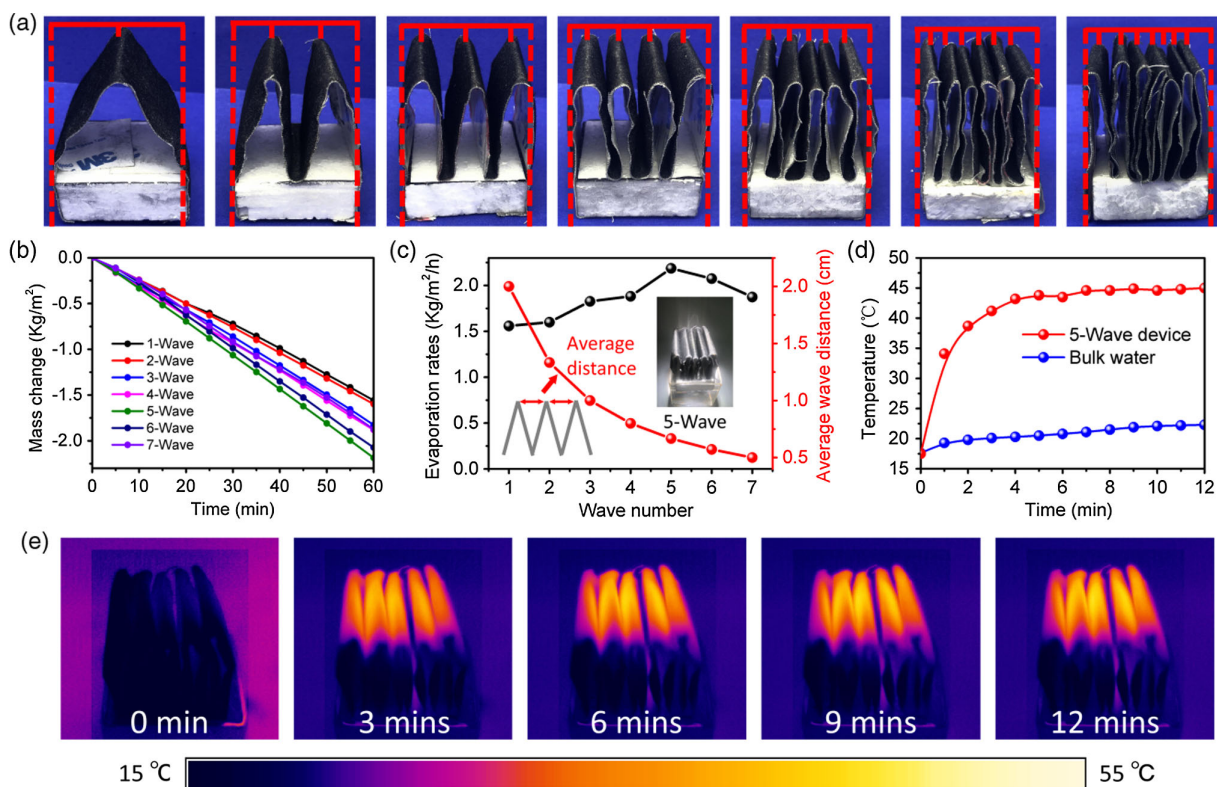

Figure 5. a) Photos of configurable wave-like 3D structures with adjustable waves. b) Mass change versus time curves of 3D structures with a series of numbers of waves. c) The evaporation rate versus numbers of waves curve. d) The temperature versus time curves of the bulk water and 3D structure with five waves. e) IR images of the 3D structure with five waves within 12 min.

sunny and the outdoor temperature was recorded per hour (Figure S11e, Supporting Information). After 9 h of distillation, the purified water for the 2D and 3D structures was both collected and calculated, resulting in 0.997 and 1.298 kg m^{-2}, respectively (Figure S11f, Supporting Information). Note that the calculated values for both 2D and 3D structures in outdoor experiments are prominently lower than that in the lab. This may be due to high humidity in the sealed evaporation chambers, which can severely weaken water evaporation. In addition, the fogged roof of the chamber can also reduce the incident sunlight intensity, resulting in decreased evaporation efficiency. Specifically, when the simulated seawater was used to conduct the evaporation tests in the lab and outdoor environment, no apparent salt aggregation was observed during the whole evaporation process ranging from 1 to 9 h. The phenomenon may result from the favorable capability of water absorption for cotton fabric-based photothermal materials.[40] Additionally, enough salt particles were added onto the surface of the 2D structure that was immersed into simulated seawater with NaCl concentration of 3.5 wt% until the structure reached to a saturation state.[41] As shown in Figure S12, Supporting Information, to simulate the night environment, the abovementioned system was kept in a dark place. After 12 h, no remarkable salt particles were found

on the surface of the 2D structure, demonstrating good salt-rejecting properties

Moreover, to further achieve the detection function, CNT films with a porous network have provided an active platform to receive AuNP films to dramatically enhance SERS.[42] As the close-packed AuNP film can realize both the highly sensitive detection of water pollutants and effective photo-to-thermal conversion, it has been previously deposited on anodized nanoporous alumina template and used to construct a dual functional device for solar vaporization and pollutant detection.[29] Although we have reached significant advancement, it is still challenging due to rigid substrates, limited size, and high cost. Specifically, porous structure can function as an enhanced SERS substrate to efficiently improve SERS performance. In our system, the —COOH-functionalized CNT film-modified cotton cloth was preliminarily decorated with PEI to receive positive charges under acidic conditions (**Figure 6**a). The AuNPs with an average diameter of 35 nm were synthesized according to our reported method.[43,44] The synthesized AuNPs with red color were characterized by the UV−Vis absorption spectrum (Figure S13a,b, Supporting Information). Subsequently, a liquid/liquid self-assembly strategy was used to achieve a uniform AuNP film at the hexane/water interface (Figure S13c, Supporting Information and Figure 6b).[45] The resultant AuNP film was
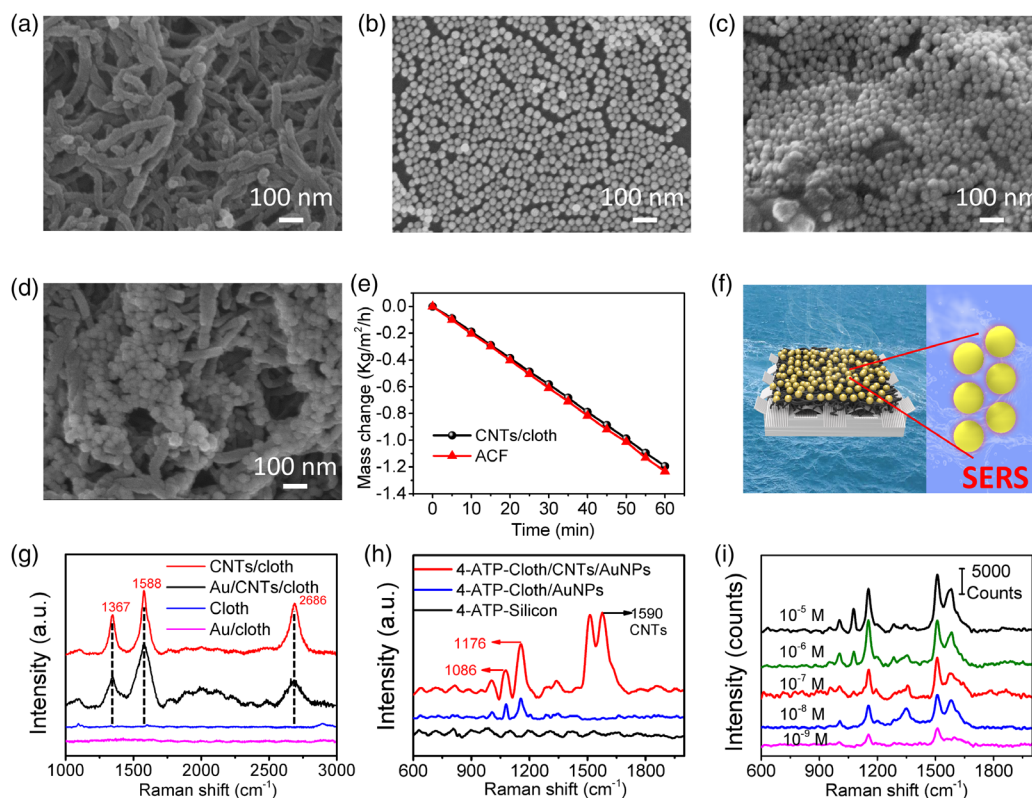
Figure 6. SEM images of a) CNT films transferred onto cotton cloth surface; b) Au monolayer film on silicon surface; and c,d) Au film transferred onto pure cotton cloth and CNT-modified cotton cloth. e) Sketch of the Au-CNTs-cloth hybrid on the water surface for SERS application. f) Mass change versus time curves of CNTs-cloth and Au-CNTs-cloth samples. g) Raman spectra of pure cloth, Au film-modified cloth, CNTs film-modified cloth, and ACF samples. h) Raman spectra of a series of samples for detecting the model molecule of 4-ATP. The dye concentration is 10^{-5} M. i) The 4-ATP detection performance of the hybrid with the lower detection limit of 10^{-9} M.

ADVANCED
SCIENCE NEWS
www.advancedsciencenews.com

Energy Technology
Generation, Conversion, Storage, Distribution
www.entechnol.de

further transferred onto the pure cotton surface as a control sample and CNT-modified cotton surface as an experimental sample. Compared with the AuNP film on the pure cotton surface, the ACF sample presented a hierarchically structured surface morphology, which was considered to effectively enhance the SERS performance due to the increased surface area and some reduced gaps between nanoparticles (Figure 6c,d).[46] From Figure 6d, it is observed that the porous network of the CNT film does not prominently cover the AuNPs.

Furthermore, the evaporation experiments were performed to investigate the effect of the AuNP film on the photo-to-thermal conversion of the achieved ACF. As shown in Figure 6e, superior to the CNT-modified cotton, the evaporation rate of the ACF represented a slight improvement. As a result, the as-prepared ACF can be attached onto the polystyrene foam for both solar vaporization and pollutant detection (Figure 6f). Moreover, Raman spectra were acquired to characterize a series of samples, including pure cotton fabric, AuNP film-modified cotton, CNT film-modified cotton, and ACF (Figure 6g). The characteristic peaks of D, G, and 2D bands could be clearly captured in the samples with the CNT film. As a proof of concept, the 4-aminothiophenol (4-ATP) with a concentration of 10^{-5} M was used to explore the detection performance of the samples. Compared with the AuNP film on the planar surface, the CNT film-enhanced AuNP film can prominently enhance the SERS performance (Figure 6h). The rough surface of the CNT network is considered to remarkably enhance SERS performance.[47] As shown in Figure S14, Supporting Information, the enhanced factors (EFs) was calculated, which reached 5.3×10^4. With the increase in irradiation time, more 4-ATP molecules were aggregated on the surface of AuNPs. As shown in Figure 6i, the detection concentration of 4-ATP reached as low as $\approx 10^{-9}$ M, demonstrating significant potential in water purification and pollutant detection.

3. Conclusion

In conclusion, we have developed an asymmetric assembly strategy to construct a configurable and SERS-active solar-driven evaporator, which can both generate purified water and detect trace pollutants in water. Considering the favorable physical and chemical properties of the cotton fabric, it was adopted to function as the active substrate to receive photothermal CNT films for a bilayer structure. The achieved fabric demonstrates excellent adjustable solar-to-thermal conversion through changing the layers of transferred CNT films. Furthermore, the flexible and foldable features of the fabric enable the configurable shapes from the 2D structure to the 3D wave-like one for efficient water evaporation. When the AuNP film was further transferred onto the PEI-modified CNTs film surface, the porous network of the CNT film effectively enhanced SERS performance. Water evaporation-induced aggregation of the model molecules of 4-ATP can remarkably optimize low-limit detection, demonstrating significant potential in the integrated devices for both pollutant detection and water purification.

4. Experimental Section

Fabrication of the CNT Film at the Air/Water Interface: CNT powders with —COOH groups (1.5 wt%) were dispersed with anhydrous ethanol,

followed by rigorous ultrasonication for 4 h. The concentration of CNT dispersion was 1 mg mL^{-1}, which was sprayed onto the water surface at an appropriate distance. When the undesirable aggregation occurred on the water surface, a porous sponge was used to compress the preassembled CNT film to a close-packed one. The resultant CNT film was further transferred onto the desired substrates.

Preparation of Patterned CNTs/Cloth Hybrid: The pure cellulose cloth fabric was rinsed with ethanol, water, and then dried in an oven. The dried cloth was folded into a square shape and covered with an additional cloth. Subsequently, the folded cloth was used to transfer the CNT film at the air/water interface from the water side. Finally, the CNT/cloth hybrid was dried in the oven to remove the absorbed water. It was noted that the transfer process was repeated several times to acquire photothermal fabrics with a series of CNT layers. The as-prepared fabric was unfolded into a patterned flat one, in which the area without CNT modification was used as the tail for water absorption. A polystyrene foam was cut into a square shape and used as the targeted substrate to receive the patterned fabric.

Formation of the Au Monolayer Film: The AuNPs were synthesized according to our previous method. The resulting AuNP solution was purified for two times via centrifugation and then put in a bottle for an appropriate volume. Subsequently, additional hexane was added onto the surface of the AuNP solution. Finally, anhydrous ethanol was slowly injected into the bottom layer of the Au solution to drive the AuNPs to have a controllable self-assembly at the liquid/liquid interface.

Preparation of ACF: Prior to the transfer of the Au film onto the CNT film, the CNT film on the fabric was preliminarily modified with the PEI polymer to interact with the AuNPs. In our experiment, the PEI aqueous solution (the MW was 70 000, 3 wt%) was dropped onto the CNT film surface and then rinsed to remove any unstable polymers. The dried PEI-modified CNT film on the fabric was finally used to transfer the Au film for all-in-one evaporators.

Water Evaporation Experiments: CNTs/cloth and ACF samples on the polystyrene foam were floated on the water surface in fixed chambers, individually, which were irradiated by a solar simulator (HM-Xe500W) equipped with the optical filter for an AM 1.5G spectrum. The mass changes were measured by an electronic balance (GXG-JJ224BC) with an accuracy of 0.0001 g at constant temperature and humidity.

SERS Measurement: The model molecule of the 4-ATP solution with a series of concentrations (10^{-5}, 10^{-6}, 10^{-7}, 10^{-8}, and 10^{-9} M) was used as the pollutant water. CNT film/cloth, AuNP film/cloth, and ACF samples were used as the solar evaporators to conduct solar steam generation under the irradiation of a solar simulator (1 kW m^{-2}). After 3 h of illumination, the resultant evaporation samples were used to conduct Raman characterization. For the blank experiment, 8 μL of the 4-ATP solution with a series of concentrations (10^{-5}, 10^{-6}, 10^{-7}, 10^{-8}, and 10^{-9} M) was respectively dropped onto the silicon wafer for Raman characterization.

Characterization: SEM (SEM Hitachi-S4800, Japan) was used to acquire the surface morphology of a series of samples. The surface temperature of the evaporators and the IR images was measured using the infrared thermal imager (TG165, FLIR, US). The Raman spectra of a series of samples were collected using a 532 nm laser and accumulated once for 10 s (1.2 mW). The Raman spectra for detecting the model molecule of 4-ATP were collected using the 532 nm laser and accumulated 15 times for 1 s (1.2 mW). (Raman Systems, Inc., R-3000 series, Britain). UV−Vis absorption spectra were recorded via a TU-1810 UV−Vis spectrophotometer (Purkinje General Instrument Company). The contact angle was determined by a contact angle meter (DCAT21), using a 3 μL droplet as an indicator. The ion concentrations of anions in the water samples were tested by inductively coupled plasma atomic emission spectroscopy (ICP-AES, NexION 300X). The reflection and transmittance spectra were recorded using a UV–Vis near-infrared spectrophotometer equipped with an integrating sphere (Lambda 950).

Supporting Information

Supporting Information is available from the Wiley Online Library or from the author.

[1] S. Sun, Y. Wang, F. Wang, J. Liu, X. Luan, X. Li, T. Zhou, P. Wu, *Sci. Rep.* **2015**, *5*, 14006.

[2] M. Elimelech, W. Phillip, *Science* **2011**, *333*, 712.

[3] M. Q. Yang, M. Gao, M. Hong, G. W. Ho, *Adv. Mater.* **2018**, *30*, 1802894.

[4] N. S. Lewis, *Science* **2016**, *351*, aad1920.

[5] L. Zhu, M. Gao, C. K. N. Peh, G. W. Ho, *Mater. Horizons* **2018**, *5*, 323.

[6] J. Kim, S. Lee, S. Kang, T. Kim, *Nanoscale* **2018**, *10*, 21555.

[7] M. Gao, L. Zhu, C. Peh, G. Ho, *Energy Environ. Sci.* **2019**, *12*, 841.

[8] P. Tao, G. Ni, C. Song, W. Shang, J. Wu, J. Zhu, G. Chen, T. Deng, *Nat. Energy* **2018**, *3*, 1031.

[9] L. Zhu, M. Gao, C. K. N. Peh, G. W. Ho, *Nano Energy* **2019**, *57*, 507.

[10] M. Zhu, Y. Li, F. Chen, X. Zhu, J. Dai, Y. Li, Z. Yang, X. Yan, J. Song, Y. Wang, E. Hitz, W. Luo, M. Lu, B. Yang, L. Hu, *Adv. Energy Mater.* **2018**, *8*, 1701028.

[11] L. Zhou, Y. L. Tan, J. Y. Wang, W. C. Xu, Y. Yuan, W. S. Cai, S. N. Zhu, J. Zhu, *Nat. Photonics* **2016**, *10*, 393.

[12] P. Alvarez, C. Chan, M. Elimelech, N. Halas, D. Villagran, *Nat. Nanotechnol.* **2018**, *13*, 634.

[13] J. Chen, J. Feng, Z. Li, P. Xu, X. Wang, W. Yin, M. Wang, X. Ge, Y. Yin, *Nano Lett.* **2019**, *19*, 400.

[14] H. Li, Y. He, Z. Y. Liu, B. C. Jiang, Y. M. Huang, *Energy* **2017**, *139*, 210.

[15] M. Gao, C. K. Peh, H. T. Phan, L. Zhu, G. W. Ho, *Adv. Energy Mater.* **2018**, *8*, 1800711.

[16] Y. Wang, L. Zhang, P. Wang, *ACS Sustainable Chem. Eng.* **2016**, *4*, 1223.

[17] Y. Liu, J. Chen, D. Guo, M. Cao, L. Jiang, *ACS Appl. Mater. Interfaces* **2015**, *7*, 13645.

[18] P. Zhang, J. Li, L. Lv, Y. Zhao, L. Qu, *ACS Nano* **2017**, *11*, 5087.

[19] Y. Li, T. Gao, C. Chen, Z. Yang, Y. Kuang, C. Jia, J. Song, E. M. Hitz, B. Liu, H. Huang, J. Yu, B. Yang, L. Hu, *Small Methods* **2018**, *3*, 1800176.

[20] X. Yang, Y. Yang, L. Fu, M. Zou, Z. Li, A. Cao, Q. Yuan, *Adv. Funct. Mater.* **2018**, *28*, 1704505.

[21] Y. Yang, R. Zhao, T. Zhang, K. Zhao, P. Xiao, Y. Ma, P. M. Ajayan, G. Shi, Y. Chen, *ACS Nano* **2018**, *12*, 829.

[22] H. C. Yang, Z. Chen, Y. Xie, J. Wang, J. W. Elam, W. Li, S. B. Darling, *Adv. Mater. Interfaces* **2018**, *6*, 1801252.

[23] L. Zhang, B. Tang, J. Wu, R. Li, P. Wang, *Adv. Mater.* **2015**, *27*, 4889.

[24] Z. Zhang, P. Mu, J. He, Z. Zhu, H. Sun, H. Wei, W. Liang, A. Li, *Chem. Sus. Chem. Eng.* **2019**, *12*, 426.

[25] Z. J. Xia, H. C. Yang, Z. Chen, R. Z. Waldman, Y. Zhao, C. Zhang, S. N. Patel, S. B. Darling, *Adv. Mater. Interfaces* **2019**, *6*, 1900254.

[26] J. Liu, Q. Liu, D. Ma, Y. Yuan, J. Yao, W. Zhang, H. Su, Y. Su, J. Gu, D. Zhang, *J. Mater. Chem. A* **2019**, *7*, 9034.

[27] N. Xu, X. Hu, W. Xu, X. Li, L. Zhou, S. Zhu, J. Zhu, *Adv. Mater.* **2017**, *29*, 1606762.

[28] Y. Bian, Q. Du, K. Tang, Y. Shen, L. Hao, D. Zhou, X. Wang, Z. Xu, H. Zhang, L. Zhao, S. Zhu, J. Ye, H. Lu, Y. Yang, R. Zhang, Y. Zheng, S. Gu, *Adv. Mater. Technol.* **2018**, *4*, 1800593.

[29] C. Chen, L. Zhou, J. Yu, Y. Wang, S. Nie, S. Zhu, J. Zhu, *Nano Energy* **2018**, *51*, 451.

[30] P. Xiao, J. Gu, C. Wan, S. Wang, J. He, J. Zhang, Y. Huang, S.-W. Kuo, T. Chen, *Chem. Mater.* **2016**, *28*, 7125.

[31] P. Xiao, Y. Liang, J. He, L. Zhang, S. Wang, J. Gu, J. Zhang, Y. Huang, S. W. Kuo, T. Chen, *ACS Nano* **2019**, *13*, 4368.

[32] Y. Liang, J. Shi, P. Xiao, J. He, F. Ni, J. Zhang, Y. Huang, C. F. Huang, T. Chen, *Chem. Commun.* **2018**, *54*, 12804.

[33] S. Hong, Y. Shi, R. Li, C. Zhang, Y. Jin, P. Wang, *ACS Appl. Mater. Interfaces* **2018**, *10*, 28517.

[34] X. Li, X. Min, J. Li, N. Xu, P. Zhu, B. Zhu, S. Zhu, J. Zhu, *Joule* **2018**, *2*, 2477.

[35] F. Ni, P. Xiao, C. Zhang, Y. Liang, J. Gu, L. Zhang, T. Chen, *ACS Appl. Mater. Interfaces* **2019**, *11*, 15498.

[36] H. Song, Y. Liu, Z. Liu, M. H. Singer, C. Li, A. R. Cheney, D. Ji, L. Zhou, N. Zhang, X. Zeng, Z. Bei, Z. Yu, S. Jiang, Q. Gan, *Adv. Sci.* **2018**, *5*, 1800222.

[37] Y. Wang, C. Wang, X. Song, M. Huang, S. K. Megarajan, S. F. Shaukat, H. Jiang, *J. Mater. Chem. A* **2018**, *6*, 9874.

[38] X. Li, J. Li, J. Lu, N. Xu, C. Chen, X. Min, B. Zhu, H. Li, L. Zhou, S. Zhu, T. Zhang, J. Zhu, *Joule* **2018**, *2*, 1331.

[39] P. Xiao, J. He, Y. Liang, C. Zhang, J. Gu, J. Zhang, Y. Huang, S.-W. Kuo, T. Chen, *Sol. RRL* **2019**, DOI: 10.1002/solr.201900004.

[40] G. Ni, S. Zandavi, S. Javid, S. Boriskina, T. Cooper, G. Chen, *Energy Environ. Sci.* **2018**, *11*, 1510.

[41] W. Xu, X. Hu, S. Zhuang, Y. Wang, X. Li, L. Zhou, S. Zhu, J. Zhu, *Adv. Energy Mater.* **2018**, *8*, 1702884.

[42] B. Qiu, M. Xing, Q. Yi, J. Zhang, *Angew Chem.* **2015**, *54*, 10643.

[43] X. Lu, A. Dandapat, Y. Huang, L. Zhang, Y. Rong, L. Dai, Y. Sasson, J. Zhang, T. Chen, *RSC Adv.* **2016**, *6*, 60916.

[44] S. Si, W. Liang, Y. Sun, J. Huang, W. Ma, Z. Liang, Q. Bao, L. Jiang, *Adv. Funct. Mater.* **2016**, *26*, 8137.

[45] X. Lu, Y. Huang, B. Liu, L. Zhang, L. Song, J. Zhang, A. Zhang, T. Chen, *Chem. Mater.* **2018**, *30*, 1989.

[46] Y. Sun, K. Liu, J. Miao, Z. Wang, B. Tian, L. Zhang, Q. Li, S. Fan, K. Jiang, *Nano Lett.* **2010**, *10*, 1747.

[47] J. Leem, M. Wang, P. Kang, S. Nam, *Nano Lett.* **2015**, *15*, 7684.